Hybrid Magnetic Materials Based on Nitroxide Free Radicals and Extended Oxalato-Bridged Bimetallic Networks

Antonio Alberola,[a] Eugenio Coronado,*[a] Carlos Giménez-Saiz,[a] Carlos J. Gómez-García,[a] Francisco M. Romero,*[a] and Ana Tarazón[a]

Keywords: Magnetic properties / Heterometallic complexes / Hybrid materials / Radicals / Layered compounds

A series of hybrid organic-inorganic magnets of formula *p*-rad[$M^{II}Cr(ox)_3$] [M = Mn (**1**), Co (**2**), Ni (**3**), Zn (**4**)] and *m*-rad[$M^{II}Cr(ox)_3$] [M = Mn (**5**), Co (**6**)], in which *N*-methylpyridinium cations bearing a nitronyl nitroxide moiety in positions 3 (*m*-rad) or 4 (*p*-rad) of the pyridine ring coexist with the 2D honeycomb-like oxalato-bridged bimetallic lattice, has been prepared and studied by AC and DC magnetic susceptibility measurements and EPR spectroscopy. In general, the physical properties of these magnets are not altered significantly by the insertion of the nitronyl nitroxide radicals although these paramagnetic molecules seem to interact weakly with the inorganic network as demonstrated by EPR spectroscopy. Some differences can also be observed between the *p*-rad and *m*-rad series, i.e. *m*-rad derivatives have smaller values for the critical temperatures and coercive fields. We also report on the X-ray crystal structures and magnetic properties of *p*-rad[$Mn(H_2O)Cr(ox)_3$]·$2H_2O$ (**7**) and *m*-rad[$Mn(H_2O)_2Cr(ox)_3$]·$2H_2O$ (**8**), two extended oxalato-bridged compounds with new topologies. Compound **7** is antiferromagnetic and its structure is a 3D achiral lattice in which zigzag ferromagnetic MnCr chains (J/k = +0.8 K) are interconnected to form hellicoidal hexagonal channels with the cationic free radicals residing in the free space. Compound **8**, however, exhibits a ladder-like structural pattern with competing magnetic interactions and paramagnetic behaviour down to low temperatures.

Introduction

For more than fifteen years, magnetochemists have been successfully surmounting the challenge of designing and constructing new crystalline solid-state materials from molecular building blocks.[1,2] In the rational design of these compounds, the building blocks are not merely virtual units in which the crystal structure is subdivided in order to get a better understanding but, rather, they are real entities which are stable in solution and can be assembled to form a particular crystal lattice with interesting properties. The well-known concepts of structural coordination chemistry provide useful design methods for the purpose of lattice engineering, since coordination geometries are defined by strong and highly directional bonds. Fortunately, coordination chemistry also affords the basic ingredients of molecule-based magnetic materials, i.e. spin carriers (metal ions) and ligands through which magnetic interactions can occur.

The homoleptic tris(oxalatometallate) anions $[M(ox)_3]^{3-}$ (M = Cr^{III}, Fe^{III}, Ru^{III}) are rather inert metal complex ions which can be assembled with metal cations to give extended heterometallic systems.[3−5] The majority of the resultant structures are composed of edge-sharing octahedra and belong to two categories, namely a) 2D bimetallic compounds of formula A[M′M(ox)$_3$] (A = quaternary onium cation, M′ = metal) with a honeycomb-layered structure[6,7] and b) 3D homometallic compounds of formulae A[$M'_2(ox)_3$], A[M′M(ox)$_3$] or A[M′M(ox)$_3$](ClO_4) (A = $[M(bpy)_3]^{2+}$) with a cubic chiral packing.[8,9] Since the formation of each structural type depends on the use of a particular A^{m+} cation, these have been considered as templating agents for the host structure.[10] It has also been recognised that chirality plays a crucial role in this molecular recognition process, i.e. chiral tris(bipyridine) metal cations induce the spontaneous resolution of 3D chiral lattices with the same configuration as the tris(oxalatometalate) sites.[11] Cross effects (magnetochiral dichroism)[12] may arise from the combination of magnetic order and chirality in 3D oxalato-based compounds.[13] In general, multiproperty hybrid materials can be synthesised from functional A^{m+} cations which introduce an additional physical property in the magnetic system. In this context, 2D compounds containing paramagnetic decamethylferricenium species,[14,15] NLO-active molecules[16] and organic π-electron donors have been studied. The latter include the first examples of the coexistence of magnetic order and metal-like conductivity in a molecular solid.[17]

Nitronyl nitroxide (NN) radicals have become commonplace in the synthesis of purely organic magnetic materi-

[a] Institut de Ciència Molecular, Universitat de València, Dr. Moliner 50, 46100 Burjassot, Spain
Fax: (internat.) +34-963544859
E-mail: fmrm@uv.es
Supporting information for this article is available on the WWW under http://www.eurjic.org or from the author.

als[18] and mixed metal-radical magnets.[19−21] Cationic NNs of the *N*-alkylpyridinium type were reported by Awaga in combination with simple anionic metal complexes.[22−26] The same nitroxide cations have also been employed as bridging units in conjunction with the well-known bimetallic chains based on the opba ligand.[27−29] These studies prompted us to investigate the use of these free radicals as functional cations in the formation of oxalato-bridged extended bimetallic compounds. In a previous communication, we reported such a hybrid magnet based on a novel 3D achiral $[MnCr(ox)_3]^-$ lattice.[30] Herein, we extend these results to other first-row divalent metal ions. The influence of the position of the NN fragment with respect to the pyridinium ring is also discussed in this paper.

Results and Discussion

Synthesis and Characterisation: The cationic free radicals employed in this study were 1-methylpyridinium derivatives bearing an NN moiety in positions 4 (*p*-rad) or 3 (*m*-rad) of the pyridine ring (Scheme 1). They were synthesised as iodide salts by a previously described procedure.[22,23] Their reaction with $Ag_3[Cr(ox)_3]$ affords *p*(*m*)-rad$_3$[Cr(ox)$_3$] which was allowed to further react with a mixture of the corresponding metal cation, M^{2+}, and $[Cr(ox)_3]^{3-}$ to yield the family of compounds *p*(*m*)-rad[MCr(ox)$_3$]. From the study of the magnetic properties of these hybrid materials (vide infra), it became clear that they belong to the 2D type of structure.

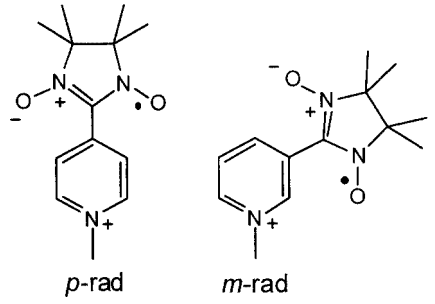

Scheme 1

$$3\,p(m)\text{-radI} + Ag_3[Cr(ox)_3] \rightarrow 3\,p(m)\text{-rad}^+ + [Cr(ox)_3]^{3-} + 3\,AgI\downarrow \quad (1)$$

$$3\,MCl_2{\cdot}nH_2O + 2\,Ag_3[Cr(ox)_3] \rightarrow 3\,M^{2+} + 2\,[Cr(ox)_3]^{3-} + 6\,AgCl\downarrow \quad (2)$$

$$3\,p(m)\text{-rad}^+ + 3\,[Cr(ox)_3]^{3-} + 3\,M^{2+} \rightarrow 3\,\text{rad}[MCr(ox)_3] \quad (3)$$

All reactions were performed in ethanol/water mixtures. The different products *p*-rad[MCr(ox)$_3$]·*n*H$_2$O [M = Mn (**1**), Co (**2**), Ni (**3**), Zn (**4**)] can be obtained in moderate yields by fast precipitation, provided that a high ethanol/water ratio and rather concentrated solutions are used in the last step. The water content was evaluated by thermogravimetric analysis for all the compounds. The same experimental conditions were applied for the synthesis of the *m*-rad series. In this case, however, the yields were lower and the radical content in the final compounds (as estimated from elemental analysis) was smaller. The deficiency of cationic radicals has to be compensated for with the absence of some $[Cr(ox)_3]^{3-}$ anions, thus increasing the M/Cr ratio. This aspect was confirmed by SEM metal analyses. Adding an excess of the free radical and/or the divalent metal resulted in compounds with the correct stoichiometry, i.e. *m*-rad[MCr(ox)$_3$]·*n*H$_2$O [M = Mn (**5**), Co (**6**)]. The corresponding Ni^{II} and Zn^{II} compounds could not be obtained, however. Clearly, the more symmetric *p*-rad cation has a stronger affinity for the 2D honeycomb lattice than *m*-rad. It seems that the formation of the hexagonal cavities around the pyridinium cation is partially hindered by the presence of the bulky NN group in the *m*-position.

The precipitation of the manganese(II)-containing products (**1** and **5**) can be avoided if reaction (3) is performed in a more aqueous and/or a more dilute solution. Under these conditions, single-crystals of the 3D *p*-rad[MnCr(ox)$_3$(H$_2$O)]·2H$_2$O (**7**) and 1D *m*-rad[MCr(ox)$_3$(H$_2$O)$_2$]·2H$_2$O (**8**) compounds could be obtained by slow evaporation. The reaction conditions are therefore critical in the synthesis of the Mn^{2+} analogues. Due to the larger size of this cation, the formation of complexes with the tris(oxalate) chromate(III) species is reduced and a competition between these anions and the solvent water molecules occurs. Under less polar and/or more concentrated conditions (kinetic control), fast precipitation occurs and the well-known 2D phases are obtained. On the other hand, increasing the water content and/or working with more dilute solutions (thermodynamic control) induces the coordination of water molecules to the Mn^{2+} ions with a complete change in the crystal structure.

Crystal Structures of 7 and 8: The hybrid salt **7** crystallises in the monoclinic space group C_c. The conformation of the *p*-rad cation (Figure 1, a) with a torsion angle of 26.6(4)° between the NN fragment and the pyridine ring is similar to that found in other salts. The packing of the free radicals (Figure 2) forms zigzag chains running along the *z*-axis. The shortest contact between proximate radicals within the chain is O2···C10 [x, 1− y, z − 1/2, 4.312(5) Å]. The N−O functions are well separated from each other with a minimum intermolecular O1···O2 (x, 1− y, z − 1/2) distance of 6.891(5) Å. This situation is special in the context of magnetic materials containing nitroxide radicals, where shorter O···O contacts of about 3.5 Å are generally observed.

The oxalato-based inorganic lattice is also shown in Figure 2 and emphasises the role of the free radicals as directing agents for the whole structure. The zigzag chain motif of the packing of NN radicals is translated to the inorganic counterpart. Indeed, the 3D bimetallic network can be viewed, in a first step, as zigzag alternating Mn−Cr chains oriented in the same direction (continuous bonds). A detailed picture of this 1D fragment is given in Figure 3 where the linkage between neighbouring metal ions by

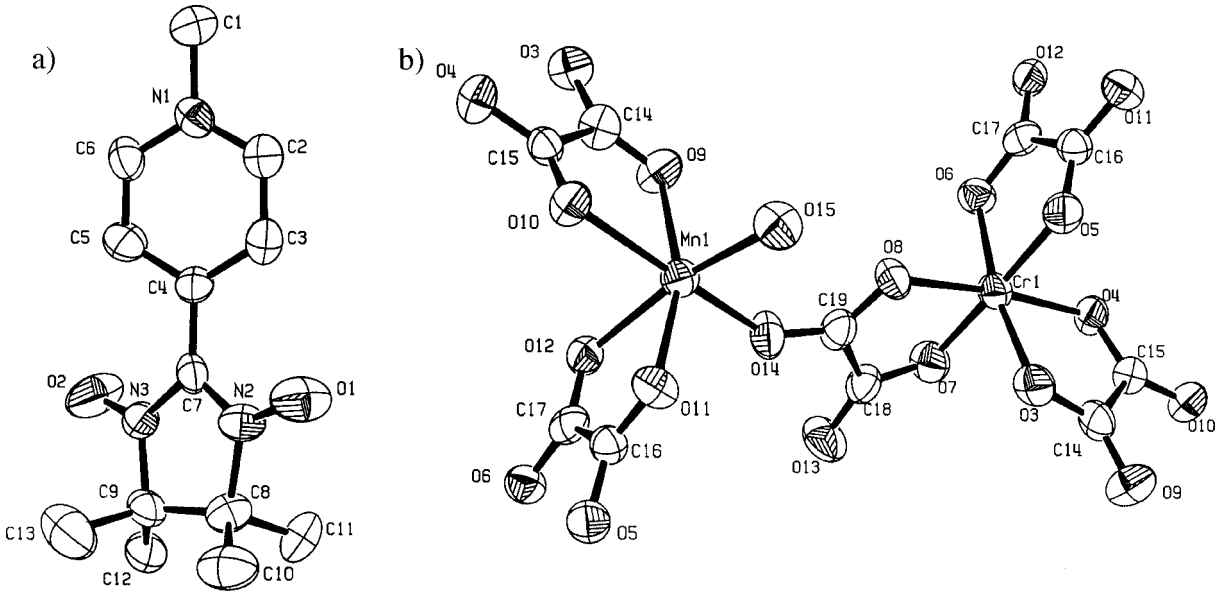

Figure 1. Molecular structure of a) *p*-rad and b) $[Mn(H_2O)Cr(ox)_3]^-$ (ellipsoids are shown at the 50% probability level; all H atoms have been omitted for clarity); selected distances (A), N2−O1 1.271(3), N3−O2 1.271(3)

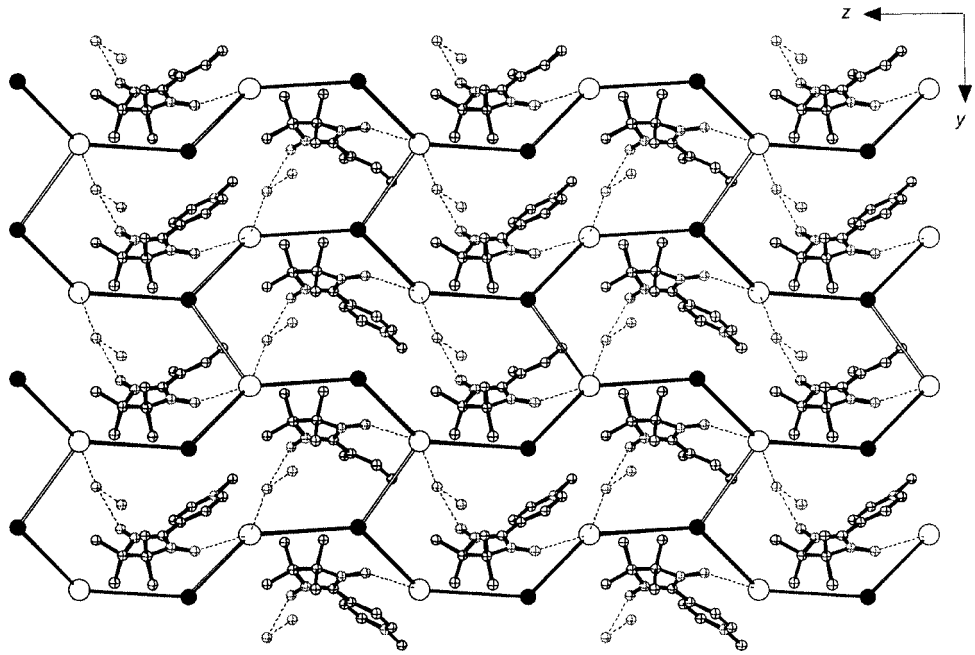

Figure 2. View of the crystal structure of **7** along the *a* axis; oxalate anions have been replaced by straight rods: black [bis(bidentate)] and white (bidentate/monodentate); dotted lines refer to hydrogen bonds, open circles = Mn, filled circles = Cr

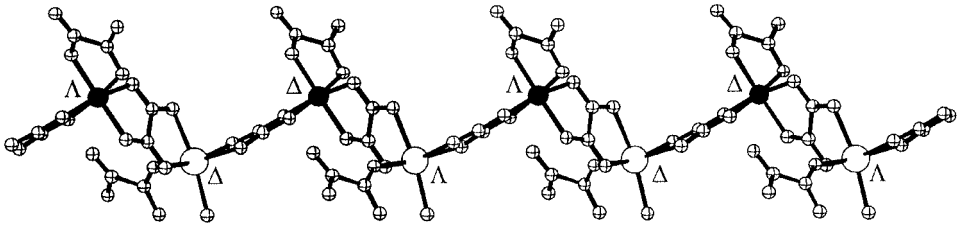

Figure 3. View along the *b* axis of the oxalato-bridged MnCr ferromagnetic chains in **7**; the absolute configuration of the metal centres is also shown, open circles = Mn, filled circles = Cr

bis(bidentate) μ-oxalate bridges can be clearly seen. In contrast to the classical 3D network built up from homochiral building blocks which combine into helical chains, the chirality of the metal centres follows the sequence ···ΔΔΛΛΔΔ··· along the chains of **7**. Two distinct bis(bidentate) bridges are then found, i.e. one connecting metal centres of the same chirality [Mn1···Cr1: 5.421(3) Å] and a second one connecting centres of opposite chirality [Mn1···Cr1 (x, 2 − y, z + 1/2): 5.3927(16) Å].

The chains are linked by a new type of oxalate bridge (see Figure 1, b) which is simultaneously bidentate (towards chromium) and monodentate (towards manganese). As expected, the metal-metal distance [Mn1···Cr1e (x + 1/2, 3/2 − y, z + 1/2): 5.5977(14) Å] is higher when compared with the bis(bidentate) bridging mode. A water molecule occupies the vacant position in the Mn^{2+} coordination sphere at a distance Mn1−O15 = 2.138(2) Å. Previous reports concerning this unusual bridging mode are very scarce.[31−33] In complex **7**, the linkage (white rods in Figure 2) takes place between $Cr(ox)_3$ and $Mn(H_2O)(ox)_3$ units of opposite chirality. This results in the formation of an achiral 3-connected decagonal network. The decagonal units are arranged out of this plane in such a way that helical hexagonal channels are formed. Since the resultant network is achiral, both types of helices are found in the structure (Figure 4).

Interestingly, the radicals are tightly bound to the inorganic lattice through an extended hydrogen-bonded network. Short hydrogen bonds are found between the nitroxide oxygen atoms and two water molecules [Mn1−O15···O2−N3 (x + 1/2, 3/2 − y, z + 1/2): 2.733(4) Å; O17···O1−N2: 2.800(3) Å]. The water molecules of crystallisation are also linked to each other [O17···O16 (x + 1, y, z): 2.762(4) Å] and are hydrogen-bonded to the coordinated water [Mn1−O15···O17: 2.674(4) Å].

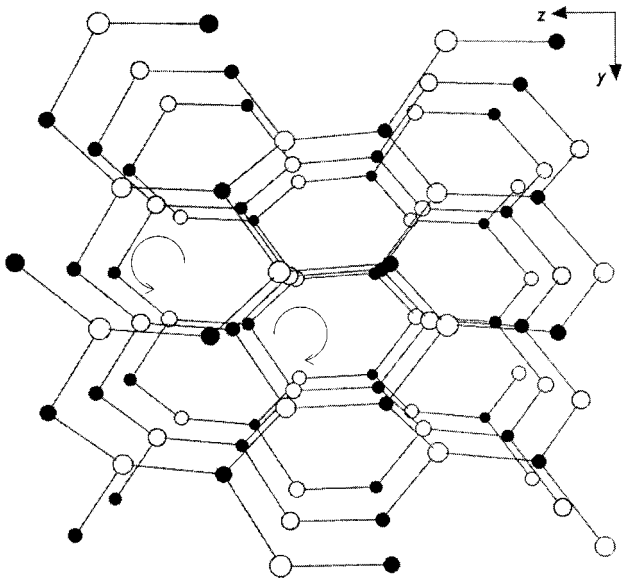

Figure 4. Perspective view along the a axis of the heterometallic lattice of **7** showing the metal connectivity and the helical channels formed; open circles = Mn, filled circles = Cr

The *m*-rad analogue **8** crystallises in the centrosymmetric $P\bar{1}$ space group. The cationic free radical (Figure 5, a) exhibits a more planar conformation with a torsion angle between the NN fragment and the pyridine ring of 15.51(10)°. The Mn^{2+} environment is markedly different with respect to **7** and only one oxalate anion now behaves in a bis(bidentate) manner with the other two (Figure 5, b) binding in the bidentate/monodentate mode occupying *trans* positions in the Mn^{2+} coordination sphere. This situation leaves two vacant *cis* positions which are occupied by water molecules. This causes the organisation of a ladder-like chain.[34−36]

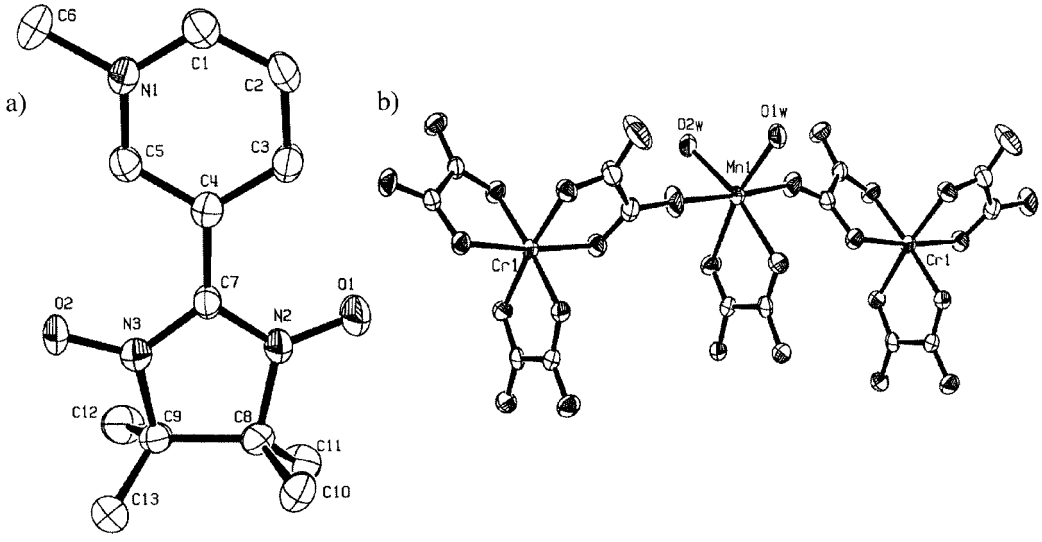

Figure 5. Molecular structure of a) *m*-rad and b) $\{Mn(H_2O)_2(ox)[Cr(ox)_3]_2\}$ fragment (ellipsoids are shown at the 50% probability level; all H atoms have been omitted for clarity); selected distances (Å): N2−O1 1.277(4), N3−O2 1.283(4)

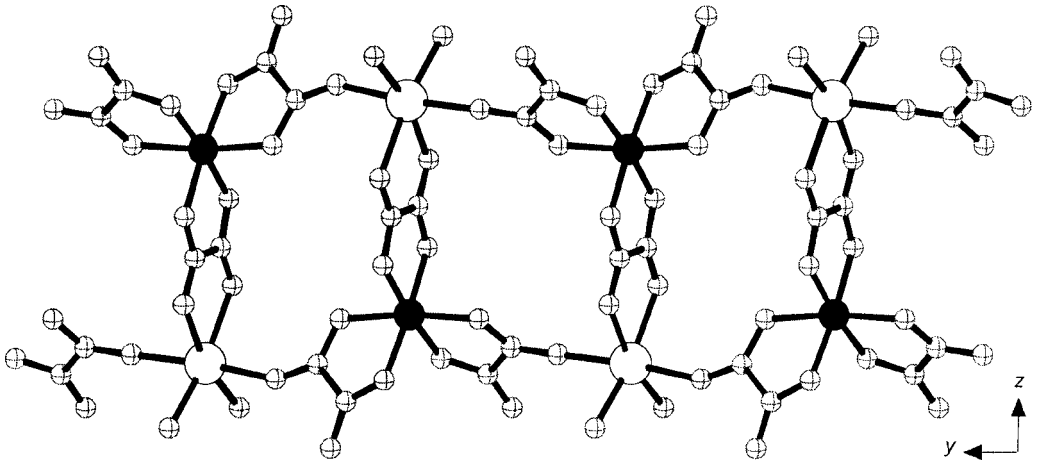

Figure 6. Projection of the crystal structure of **8** onto the *bc* plane, showing the oxalato-bridged MnCr ladder-like chains, open circles = Mn, filled circles = Cr

The steps of the ladder (Figure 6) are defined by bis(bidentate) bridges with an intermetallic distance Mn1···Cr1 = 5.4631(7) Å, while the bidentate/monodentate bridging mode propagates the lateral chains in the direction of the *b* axis. As expected, longer intermetallic distances [Cr1···Mn1($-x$ + 1, $-y$, $-z$ + 1) = 5.8370(7) Å and Mn1···Cr1($-x$ + 1, $-y$ + 1, $-z$ + 1) = 5.9902(7) Å] are found in this case. The chains are related by an inversion centre and the resultant ladder is achiral.

The free radicals (Figure 7) also form zigzag chains running along the *b*-axis. They can be viewed as chains of centrosymmetric dimers with the shortest intradimer distance of C40···C40 = 3.512(5) Å ($-x$, $-$,$-z$). The N−O moieties are even more isolated than in compound **7** and their minimum O···O distance in the crystal is 7.478(5) Å. Again, the water molecules of crystallisation are linked to each other [O3W···O4 W($-x$, 1$-$ y, 2 $-$ z) = 2.908(5) Å] and hydrogen-bonded to the coordinated water

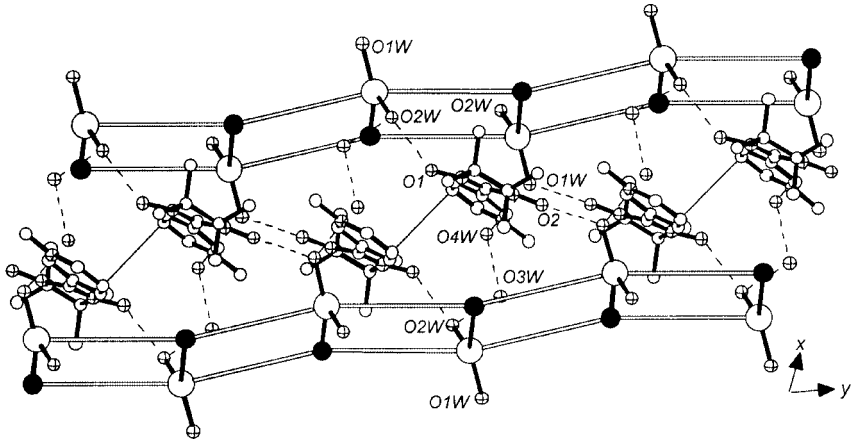

Figure 7. Projection of the crystal structure of **8** onto the *ab* plane, showing the radical zigzag chains of dimers and the oxalato-bridged ladder; oxalate anions have been replaced by straight rods: black [bis(bidentate)] and white (bidentate/monodentate); dotted lines refer to hydrogen bonds, open circles: Mn, filled circles: Cr

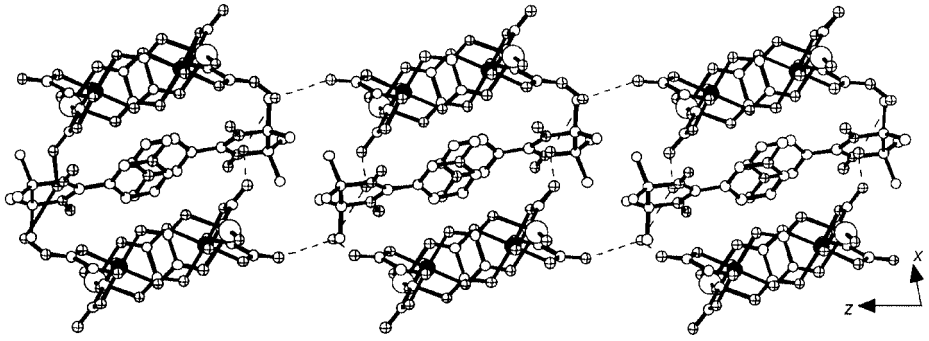

Figure 8. View along the *b* axis of the ladder-like oxalato-bridged lattice and the zigzag nitroxide chains of **8** showing the participation of the oxalate anions in hydrogen bonding; open circles: Mn, filled circles: Cr

Table 1. Magnetic parameters for the series *p*-rad[$M^{II}M^{III}(ox)_3$] and *m*-rad[$M^{II}M^{III}(ox)_3$] (**1**−**7**): critical temperature (T_c), Weiss constant (θ), Curie constant (C), saturation magnetisation (M_{sat}) and coercive field at 2 K (H_{coer})

$M^{II}M^{III}$	*p*-rad					*m*-rad				
	T_c (K)	θ (K)	C (emu·K·mol^{-1})	M_{sat} (μ_B)	H_{coer} (G)	T_c (K)	θ (K)	C (emu·K·mol^{-1})	M_{sat} (μ_B)	H_{coer} (G)
MnCr	5.7	8.0	6.13	7.74	66	5.3	7.0	6.55	7.37	17
CoCr	13.8	10.0	5.37	6.22	4400	11.3	11.0	5.24	5.17	230
NiCr	15.5	17.2	3.14	5.57	1500	–	–	–	–	–
ZnCr	–	2.8	2.29	–	–	–	–	–	–	–

[Mn1−O2W···O3 W(x, y, z − 1) = 2.688(4) Å, Mn1−O1W···O4 W(1 − x, 1 − y, 1 − z) = 2.653(4) Å]. The nitroxide functions are bonded to coordinated and free water molecules [O1···O2 W(1 − x, 1 − y,1 − z) = 2.714(4) Å; O2···O1 W(2 − x, −y, 1 − z) = 2.719(4) Å]. The free radicals are thus held in the lattice by an intricate network of hydrogen bonds.

A view parallel to the chains (Figure 8) shows how these 1D organic and inorganic units alternate in the solid-state and also emphasises the role played by the oxalate anions in stabilising additional hydrogen bonds which link the ladders along the z direction.

Magnetic Properties of the Mn-Containing Hybrid Salts (1, 5, 7−8): It is interesting to compare these CrMn bimetallic compounds since only the noncrystalline materials obtained by fast precipitation (**1** and **5**) exhibit ferromagnetic ordering. Table 1 lists the values of χT (at 300 K), magnetisation (at 5 T), the coercive field and critical temperatures for all the compounds studied in this work. At room temperature, the four CrMn hybrid salts exhibit similar values of χT which lie close to the expected values for the sum of the isolated spins [nitroxide radical (S = 1/2), Mn^{2+} (S = 5/2) and Cr^{3+} (S = 3/2) cations]. On lowering the temperature, χT continuously increases (see Supporting Information) for all the compounds, suggesting the existence of short-range ferromagnetic interactions. Compounds **1** and **5** exhibit clear indications of ferromagnetic ordering, such as the onset of out-of-phase AC susceptibility signals below 5.7 K and 5.3 K, respectively (Figure 9). Hysteresis loops with very small coercive fields (66 G for **1**, 17 G for **5**) can also be observed. Both features clearly demonstrate that **1** and **5** belong to the 2D structural family of mixed-metal oxalates. In contrast, the magnetic behaviour of compounds **7**−**8** points to the presence of competing antiferromagnetic interactions. Both hybrid salts exhibit a rounded maximum in the χT vs. T curve and **7** even shows the presence of a sharp maximum at 6 K in the χ vs. T plot, a signature of antiferromagnetic ordering. Complex **8**, however, remains paramagnetic in the whole temperature range studied.

The magnetic properties of **7**−**8** can be understood by considering the crystal structures of these hybrid metal-radical salts. All previous studies have indicated that the Mn^{II}−Cr^{III} exchange coupling through bis(bidentate) oxalate anions is ferromagnetic. Indeed, the thermal variation (Figure 10) of the χT product for **7** (at temperatures above the Néel point) is well described in terms of a regular AB ferromagnetic chain model[37] with classical spins S_A = 5/2 and S_B = 3/2 ($H_{ex} = -J\Sigma S_{Ai}S_{Bi}$).[38] The best-fit value for the exchange coupling constant is J = +0.6 cm^{-1}, a value which is in agreement with previous observations. The antiferromagnetic order is then driven by weak antiferromagnetic interactions between the chains. These interactions are certainly transmitted through the bidentate/monodentate oxalate anion. The lower symmetry of this bridge decreases the efficiency of the ferromagnetic pathway (compared with the bis(bidentate) ligand) and the antiferromagnetic term becomes dominant, as has been shown recently in a chromium-manganese tetramer.[33] Antiferromagnetic ordering is generated in the inorganic lattice and the radicals seem to remain uncoupled to this magnetically ordered network, a hypothesis which is corroborated by the presence of a

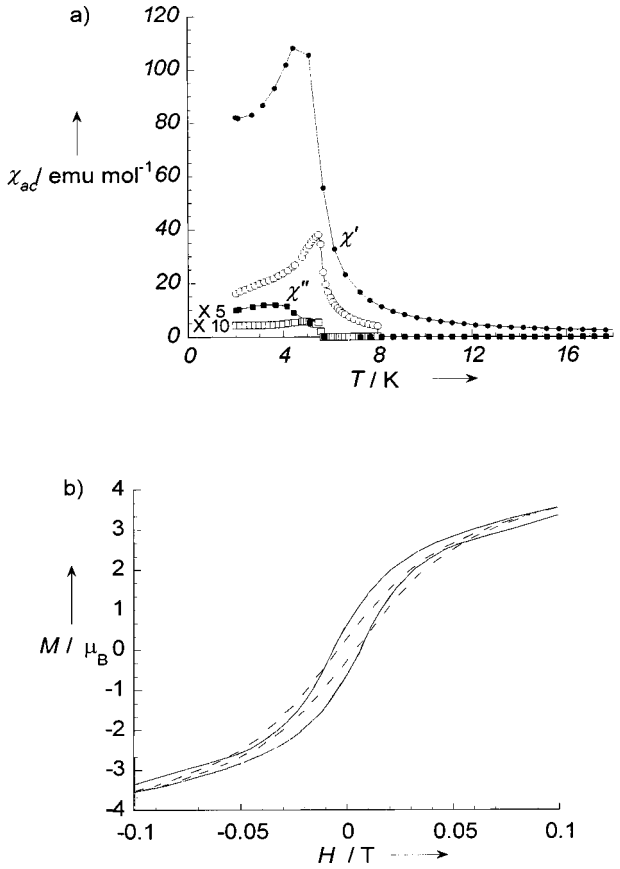

Figure 9. a) Temperature dependence of the real and imaginary components of the ac magnetic susceptibility of **1** (empty symbols, operating frequency: 1 Hz) and **5** (filled symbols, operating frequency: 110 Hz); b) low-field region of the hysteresis loops of **1** (solid line) and **5** (dashed line) measured at 2 K

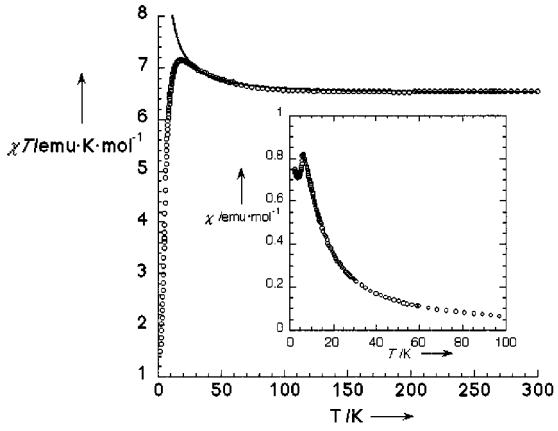

Figure 10. Thermal variation of the χT product (open circles) for **7**. The solid line represents the best-fit data for a ferromagnetic MnCr chain with $J = +0.6$ K; inset: temperature dependence of χ for the same compound

Curie tail at low temperatures. This is observed despite the fact that the nitroxide oxygen atom is hydrogen-bonded to the coordinated water molecule and, consequently, close to the manganese centre [Mn1···O2 ($x + 1/2$, $3/2 - y$, $z + 1/2$) = 3.8510(27) Å]. It seems that the magnetic interaction through this bridge is too weak to be appreciated in the temperature range of study.

The magnetostructural correlations found for complex **7** (ferromagnetic interaction transmitted through bis(bidentate) oxalate anions and antiferromagnetic coupling mediated via the asymmetric bridge) suggest the use of a spin-ladder chain model with competing interactions for the analysis of the magnetic properties of **8**.[39] Ferromagnetic interactions take place in the steps of the ladder, while the antiferromagnetic coupling propagates along the rungs, giving rise to a diamagnetic ground state. The free radicals can be considered as an independent paramagnetic contribution, as for **7**. In the absence of an exact solution for this system, the ladder chain can be approximated to a cluster-type model of isotropic spins (Figure 11).[40] The best-fit data for the two magnetic coupling parameters are $J = +0.8$ cm^{-1} and $j = -0.35$ cm^{-1}. As expected, the positive interaction is of the same order of magnitude as that estimated for the *p*-rad analogue.

Magnetic Properties of the Co-Containing Hybrid Salts (2 and 6): At room temperature, the value of χT for **2** (Figure S2a, see Supporting Information and the corresponding footnote on the first page of this article) is 5.88 emu·K·mol^{-1}. Subtraction of the radical and chromium(III) contributions leads to a reasonable value of 3.63 emu·K·mol^{-1} per cobalt(II) centre. On lowering the temperature, χ increases and eventually reaches saturation at a high value of 16.8 emu·K·mol^{-1} at 2.1 K, suggesting ferromagnetic ordering at low temperatures. Confirmation of the magnetic order (Figure 12) is provided by the observation of an out-of-phase signal in the AC susceptibility measurements below $T_C = 13.8$ K. Magnetisation hysteresis loops can be observed below this temperature with very high coercive field values ($H_{coer} = 4400$ G at 2 K) compared with those previously reported for CoCr oxalato-bridged 2D magnets. Saturation is almost reached in a 5 T field with a magnetisation value of 6.2 μ_B.

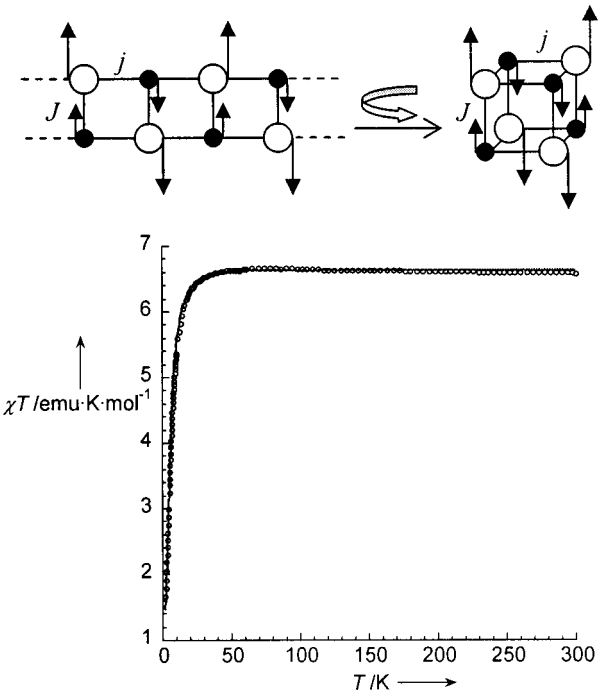

Figure 11. Top: 8-spin ring cubane model adopted for the spin-ladder chain; bottom: thermal variation of the χT product (open circles) for **8**; the solid line represents the best-fit data ($J = +0.8$ cm^{-1}; $j = -0.35$ cm^{-1})

Compound **6** exhibits (Figure S2b, Supp. Inf.) a room-temperature χT value of 5.52 emu·K·mol^{-1}. Taking into account the contributions of the radical and chromium(III) centres, a value of 3.27 emu·K·mol^{-1} per cobalt(II) centre can be calculated. This is close to the expected value for a free Co^{2+} ion showing orbital degeneracy. χ increases continuously on cooling and undergoes saturation with a value of 17.2 emu·K·mol^{-1} at 2 K. Compounds **2** and **6** show a similar thermal dependence in the DC susceptibility. The AC data, however, show clear differences between the *p*-rad and *m*-rad derivatives. The latter orders ferromagnetically at $T_C = 11.3$ K and exhibits a rounded maximum in the thermal dependence of the in-phase component. This is in contrast to the extremely sharp peak observed for the *p*-rad analogue (**6**). Also, field-dependent studies show a much smaller coercive field ($H_{coer} = 230$ G at 2 K) compared with that in **2**. The different magnetic behaviour of both compounds may be ascribed to the presence of metal defects and/or disorder in the *m*-compound which push the T_C to lower temperatures. The differences in coercive field values may also be explained in terms of a different morphology of the samples: The *p*-rad derivative (**2**) has an unusually large particle size (8 μm) compared with the other compounds (the particle size of **6** is 250 nm).

Magnetic Properties of the Ni-Containing Hybrid Salt (3): The value of χT at 300 K for **3** (3.53 emu·K·mol^{-1}) is slightly higher than the sum of the paramagnetic contri-

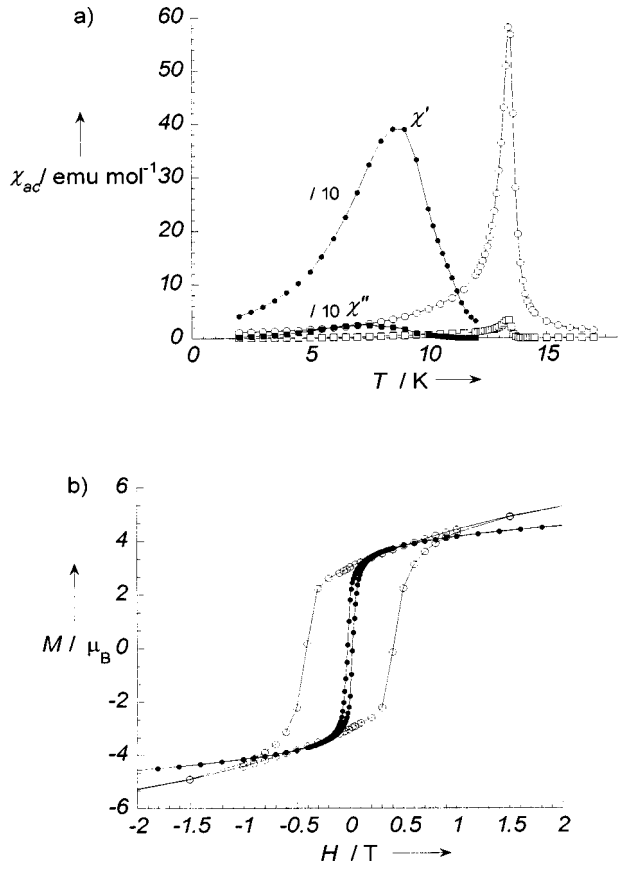

Figure 12. a) Temperature dependence of the real and imaginary components of the ac magnetic susceptibility of **2** (empty symbols) and **6** (filled symbols); operating frequency: 110 Hz; b) low-field region of the hysteresis loops of **2** (empty symbols) and **6** (filled symbols) measured at 2 K

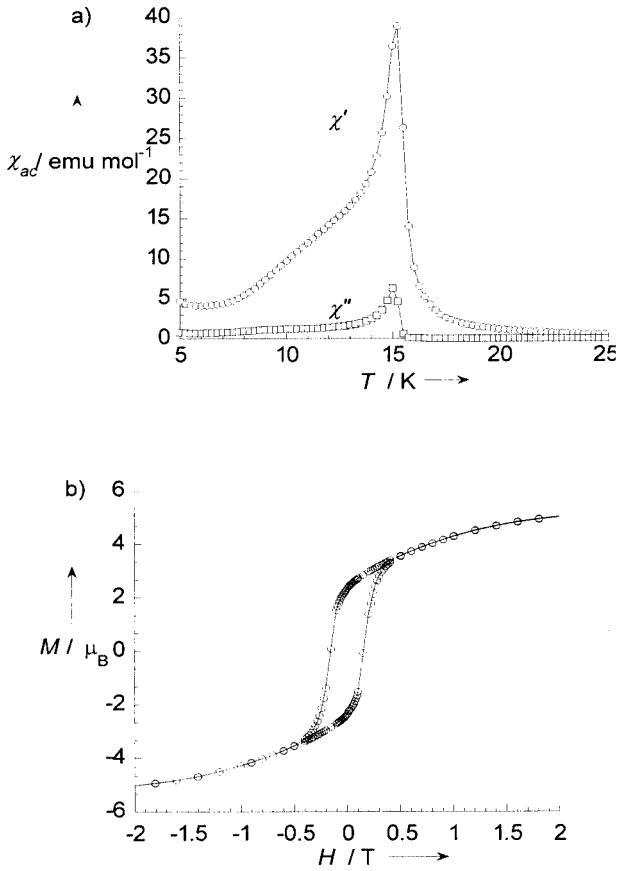

Figure 13. a) Temperature dependence of the real and imaginary components of the ac magnetic susceptibility of **3**; operating frequency: 110 Hz; b) low-field region of the hysteresis loops of **3** measured at 2 K

butions of the different spin carriers (Figure S3, Supp. Inf.). χ increases considerably upon cooling, indicating the presence of a ferromagnetically ordered phase at low temperatures. The onset of an out-of-phase signal in the AC susceptibility (Figure 13) measurements below T_C = 15.5 K provides further evidence of magnetic order. Again, magnetisation hysteresis loops were observed with very high coercive field values (H_{coer} = 1500 G at 2 K) compared with those previously reported for NiCr oxalato-bridged 2D magnets. Saturation is almost reached in a 5 T field with a magnetisation value of 5.6 μ_B.

Magnetic Properties of the Zn-Containing Hybrid Salt (4): This product exhibits room-temperature χT values that lie close to the sum of the calculated contributions for isolated Cr^{III} and free radical units. χT remains practically constant (Figure 14) upon cooling down to 10 K. Below this point, χT increases constantly upon decreasing the temperature, indicating that an intermolecular ferromagnetic interaction between radicals may also be present. In the absence of structural characterisation, it is difficult to ascribe this behaviour to particular intermolecular contacts so that an interaction between the free radical and the chromium(III) centres cannot be ruled out. The field dependence of the magnetisation shows typical Brillouin behaviour. As quoted in Table 1, saturation is not reached in a 5 T field.

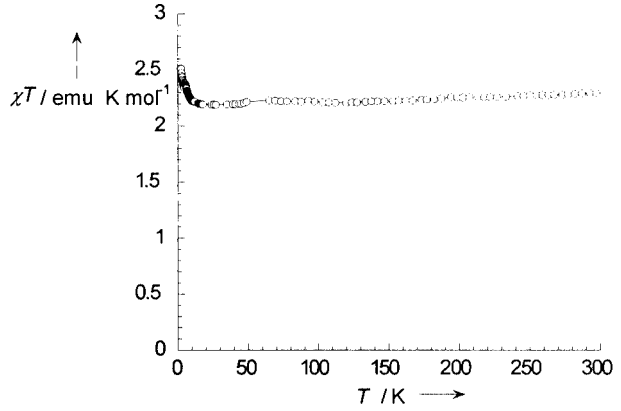

Figure 14. Thermal variation of χT for compound **4** measured in a 0.1 T field

EPR Spectroscopy: The magnetic transitions of the different compounds can be monitored by EPR spectroscopy. At room temperature, the EPR spectrum (Figure 15) of the paramagnetic derivative *p*-rad[ZnCr(ox)$_3$] (**4**) can be viewed as the sum of the contributions of the different spin carriers in the lattice. An asymmetric signal can be observed with a maximum at g = 4.1. This signal is characteristic of the $[Cr(ox)_3]^{3-}$ fragment with a zero-field splitting of the ground state.[41] In the g = 2.0 region, the expected free

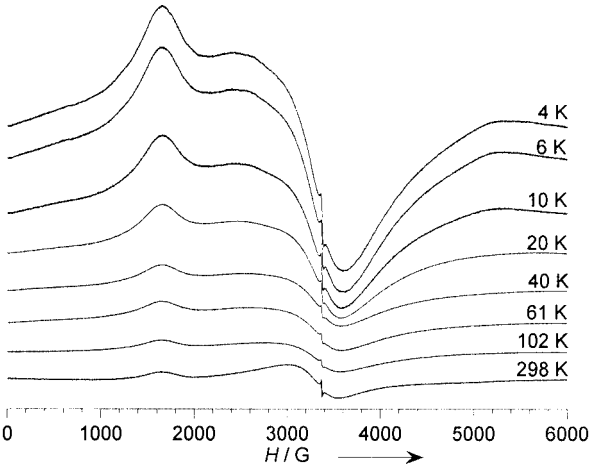

Figure 15. EPR spectra of *p*-rad[$ZnCr(ox)_3$] (**4**) at different temperatures

radical signal is superimposed with a weak contribution which originates from the chromium(III) centres. This feature is relatively broad (g = 2.057; ΔH_{pp} = 560 G) compared with previously reported salts based on *p*-rad (dipolar broadening). On lowering the temperature, the signal continuously broadens and becomes more asymmetric. At 3.2 K, the peak-to-peak width ΔH_{pp} is equal to 1130 G. A nitroxide impurity can be seen in the whole-temperature range at g = 2.005.

On the other hand, the EPR spectrum at room temperature (Figure 16) of *p*-rad[$MnCr(ox)_3$]·H_2O (**1**) shows a single line centred at g = 1.996 with a peak-to-peak width ΔH_{pp} = 350 G. The asymmetric signal of the chromium(III) moiety and the characteristic peak of the free radical are not observed. On lowering the temperature, the intensity of the signal increases and broadens to a peak-to-peak width value of 900 G at 7.6 K. Below the critical temperature, the signal splits into two components centred at g = 1.44 and g = 4.52 G. These features parallel the previously reported data for [$FeCp^*_2$][$MnCr(ox)_3$]. In this case, however, the free radical does not show an intrinsic signal, indicating exchange interactions between the two magnetic sublattices.

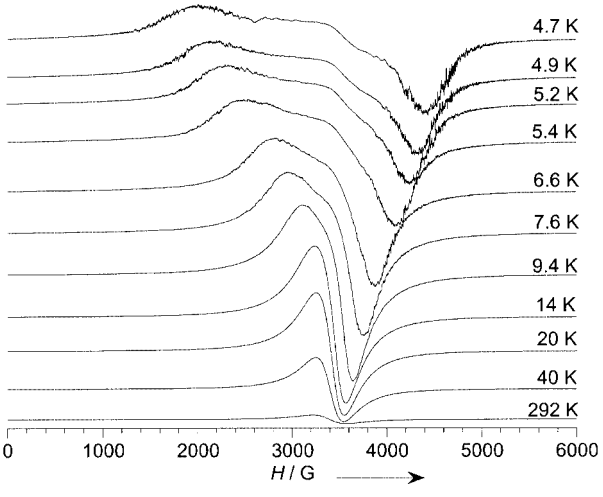

Figure 16. EPR spectra of *p*-rad[$MnCr(ox)_3$]·H_2O (**1**) at different temperatures

The temperature dependence (Figure 17) of the EPR properties of the antiferromagnetic compound *p*-rad[$Mn(H_2O)Cr(ox)_3$]·$2H_2O$ (**7**) was investigated to allow comparison with the 2D ferromagnetic isomer *p*-rad[$MnCr(ox)_3$]·H_2O (**1**). The experiment was performed on a collection of single crystals. At room temperature, the EPR spectrum of **7** also shows a single line centred at the same g-value (1.996) with a peak-to-peak width ΔH_{pp} = 420 G. On lowering the temperature, the intensity of the signal increases, reaches a maximum around 12 K. It then decreases and broadens to a peak-to-peak width value of 560 G at 7.9 K. Below the Néel temperature the signal decreases dramatically, as expected for an antiferromagnetic ordered phase. A very weak anisotropic signal remains at low temperature which can be ascribed to the radical contribution and possible traces of chromium(III).

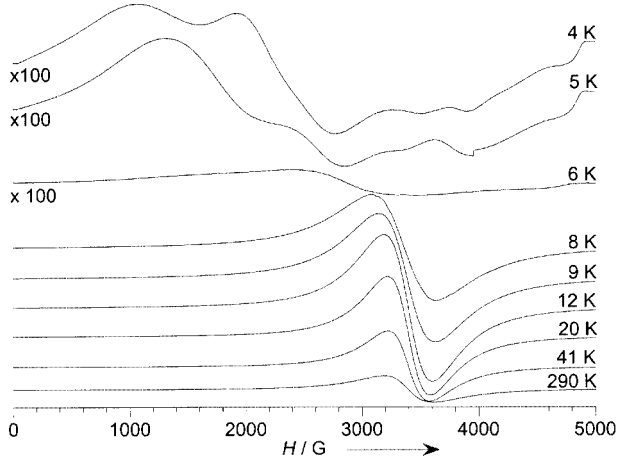

Figure 17. EPR spectra of *p*-rad[$Mn(H_2O)Cr(ox)_3$]·$2H_2O$ (**7**) at different temperatures

The EPR spectrum (Figure S4) of *p*-rad[$CoCr(ox)_3$]·$2H_2O$ (**2**) at room temperature is essentially featureless. The presence of the orbitally degenerate Co^{2+} cation induces a fast spin relaxation at high temperatures. Below 60 K, a broad and asymmetric feature appears at g = 1.54. On decreasing the temperature further, the signal becomes more intense and shifts slowly upfield. Below T_C, the main feature is accompanied by a small hump at very low fields which can be attributed to ferromagnetic resonance.

The temperature dependence of the EPR spectrum (Figure S5) for *p*-rad[$NiCr(ox)_3$]·H_2O (**3**) is similar to that observed for **1**. Only one broader signal (ΔH_{pp} = 1230 G) centred at g = 2.049 can be detected in the paramagnetic regime (the sharp line at g = 2.005 can be ascribed to a nitroxide impurity representing less than 0.01%). This is again an indication of the exchange interaction between the free radical and the magnetic network. At temperatures close to T_C, the main feature becomes anisotropic and a low-field component appears. This signal shifts downfield at a high rate (700 G/K) when decreasing the temperature, indicating the rise of the internal field in the solid.

As expected, the systematic study of the EPR spectra reveals drastic changes which occur close to T_C for all the magnetically ordered compounds. In general, the shift of the radical resonance below the ordering temperature could be used to monitor the strength of the internal magnetic field. This has been the case in hybrid metal-radical layered systems of the brucite type[42] or in the family of compounds $[FeCp^*_2][MM'(ox)_3]$. In our case, however, the radical is not merely a spectator since it couples with the anionic lattice by exchange interactions. Compared with the decamethylferricenium derivative, where most of the spin density is located in the iron centre and hence sandwiched by Cp* molecules, the nitroxide radical is less protected from the surroundings and it can readily interact with the neighbouring spin carriers.

Conclusion

The ability of cationic nitronyl nitroxide type free radicals to act as countercations of oxalato-bridged bimetallic compounds has been studied in this work. Hybrid materials which combine nitroxide free radicals and ferromagnetic layers with similar magnetic properties as those previously observed in the quaternary onium analogues $[AR_4][MCr(ox)_3]$ (A = N, P) have been obtained. The syntheses of the latter proceed in high yield by fast precipitation in aqueous solutions due to the nonpolar character of the tetrabutylammonium or tetraphenylphosphonium cations. In our case, the presence of the radical moiety confers high polarity on the cation, solvation becomes more effective and precipitation of the extended compound is hindered. This is particularly the case for M = Mn (and also Zn) since the tris(oxalate)chromate(III) ligand has a lower affinity for this larger cation. Working in concentrated conditions and in less polar solvents (ethanol/water mixtures) invariably affords the hybrid 2D magnets as fine powders (*kinetic control*) while performing the syntheses in more dilute aqueous solutions (*thermodynamic control*) yields new heterodimetallic oxalato-based lattices which result from partial occupation, by water molecules, of the vacant positions of the divalent metal. We have shown that the size and shape of the free radical determines the geometry and dimensionality of these novel hybrid materials: *p*-rad stabilizes a 3D achiral network of hellicoidal hexagonal channels, while *m*-rad acts as countercation to a ladder-like anionic structure. The influence of the free radical in the structure of the inorganic host is made possible by the formation of hydrogen bonds which involve adventitious solvent molecules.

This family of compounds, in which ferromagnetic layers coexist with free radical species, can be considered as multifunctional hybrid magnets such as those based on the paramagnetic decamethylferricinium cation $[FeCp^*][M^{II}M^{III}(ox)_3]$. As was observed in this previously reported example, the paramagnetic cation (in this case, the nitronyl nitroxide free radical) has little influence on the ordering temperatures but has a marked effect on the coercive field values, although this effect can be correlated with other features such as the particle size. Both magnetic parameters (critical temperatures and coercive fields) are similar to those found in other families of 2D oxalate-based magnets with low T_C (around 5 K) and H_{coer} values for the Mn-containing compounds and higher ordering temperatures (11−15 K) for the Ni and Co complexes. The most important difference between the two families of hybrid magnets is that whereas the two magnetic sublattices are quasi-independent in $[FeCp^*][M^{II}M^{III}(ox)_3]$, a sizeable interaction between the free radicals and the inorganic layers has been indicated by EPR spectroscopic studies in the present case.

Further work on this topic will be directed towards the preparation of nitronyl nitroxide cationic free radicals based on tetraalkylammonium salts which can be more efficient templates of the 2D hexagonal oxalate-based network.

Experimental Section

General Procedure for the Preparation of Hybrid Magnets 1−6: $Ag_3[Cr(ox)_3]$ (0.08 mmol) was added to a solution of the cationic free radical (prepared as the iodide salts *p*-radI or *m*-radI) (0.25 mmol) in EtOH (5 mL, 96%) and H_2O (1 mL). After 30 min stirring, AgI was removed by centrifugation. In a separate beaker, a solution of $[M(H_2O)_n]Cl_2$ (M = Mn, Co, Ni, Zn) (0.25 mmol) in EtOH (5 mL, 96%) and H_2O (1 mL) was allowed to react with $Ag_3[Cr(ox)]_3$ (0.17 mmol). After stirring for 30 min, AgCl was removed by centrifugation. The two supernatant solutions were mixed and the precipitated green powder was collected by centrifugation.

***p*-rad[MnCr(ox)$_3$]·H$_2$O (1):** Yield: 121 mg (75%). IR (KBr): $\tilde{\nu}$ = 1631 (CO), 1373 (NO), 1143 cm^{-1} (NO). $C_{19}H_{21}CrMnN_3O_{15}$ (638.3): calcd. C 35.75, H 3.32, N 6.58; found C 35.23, H 3.24, N 6.02.

***p*-rad[CoCr(ox)$_3$]·2H$_2$O (2):** Yield: 107 mg (65%). IR (KBr): $\tilde{\nu}$ = 1626 (CO), 1377 (NO), 1137 cm^{-1} (NO). $C_{19}H_{23}CoCrN_3O_{16}$ (660.3): calcd. C 34.56, H 3.51, N 6.36; found C 34.36, H 3.21, N 6.16.

***p*-rad[NiCr(ox)$_3$]·H$_2$O (3):** Yield: 98 mg (61%). IR (KBr): $\tilde{\nu}$ = 1623 (CO), 1377 (NO), 1139 cm^{-1} (NO). $C_{19}H_{21}CrN_3NiO_{15}$ (642.1): calcd. C 35.54, H 3.30, N 6.54; found C 35.73, H 3.37, N 6.61.

***p*-rad[ZnCr(ox)$_3$] (4):** Yield: 102 mg (64%). IR (KBr): $\tilde{\nu}$ = 1629 (CO), 1384 (NO), 1137 cm^{-1} (NO). $C_{19}H_{19}CrN_3O_{14}Zn$ (630.7): calcd. C 36.18, H 3.04, N 6.66; found C 37.15, H 3.63, N 7.21.

***m*-rad[MnCr(ox)$_3$]·H$_2$O (5):** Yield: 96 mg (55%). IR (KBr): $\tilde{\nu}$ = 1653 (CO), 1383 (NO), 1139 cm^{-1} (NO). $C_{19}H_{21}CrMnN_3O_{15}$ (638.3): calcd. C 35.75, H 3.32, N 6.58; found C 36.14, H 3.51, N 6.76.

***m*-rad[CoCr(ox)$_3$]·H$_2$O (6):** Yield: 94 mg (69%). IR (KBr): $\tilde{\nu}$ = 1628 (CO), 1377 (NO), 1137 cm^{-1} (NO). $C_{19}H_{21}CoCrN_3O_{15}$ (642.3): calcd. C 35.53, H 3.30, N 6.54; found C 35.13, H 3.48, N 6.37.

Preparation of 7−8: The cationic free radical (*p*-radI or *m*-radI) (100 mg, 0.26 mmol) was added to a suspension of $Ag_3[Cr(ox)_3]$ in EtOH (5 mL). After 30 min stirring, AgI was filtered and a solution of $Mn(ClO_4)_2·6H_2O$ (32 mg, 0.088 mmol) in a minimum amount of water was added to the filtrate. The resultant green suspension became clear after addition of H_2O (2 mL) and the mixture was

left undisturbed in the dark. Green single crystals suitable for X-ray structure analysis appeared within a few hours.

***p*-rad[MnCr(ox)$_3$(H$_2$O)]·2H$_2$O (7):** Yield: 94 mg (60%). IR (KBr): $\tilde{\nu}$ = 1630 (CO), 1376 (NO), 1140 cm^{-1} (NO). $C_{19}H_{25}CrMnN_3O_{17}$ (674.3): calcd. C 33.84, H 3.74, N 6.23; found C 33.73, H 3.75, N 6.14.

***m*-rad[MnCr(ox)$_3$(H$_2$O)$_2$]·2H$_2$O (8):** Yield: 96 mg (62%). IR (KBr): $\tilde{\nu}$ = 1634 (CO), 1378 (NO), 1139 cm^{-1} (NO). $C_{19}H_{27}CrMnN_3O_{18}$ (692.4): calcd. C 32.96, H 3.93, N 6.07; found C 32.78, H 3.86, N 6.19.

Physical Measurements: All magnetic measurements were carried out on powdered samples with a Quantum Design MPMS-XL-5 SQUID magnetometer. Variable temperature susceptibility measurements were carried out on polycrystalline samples in the 2−300 K temperature range at a magnetic field of 0.1 T. Diamagnetic contributions were corrected with Pascal's constants. Isothermal magnetisation measurements were collected in the H = 0−5 T field range at 2 K. The hysteresis studies were performed between 5 and −5 T, at 2 K, cooling the samples at zero field. AC measurements were performed at different frequencies with an oscillating magnetic field of 0.395 mT. The ESR spectra were recorded on powdered samples in the X-band region (ν = 9.47 GHz) with a Bruker E500 ELEXSYS spectrometer equipped with a helium cryostat in order to study the thermal dependence in the temperature range 300−3 K. IR transmission measurements of pressed KBr pellets were recorded at room temperature with a Nicolet Avatar 320 FT-IR spectrophotometer in the range 4000−400 cm^{-1}. CHN elemental analyses were carried out with a CE instruments EA 1110 CHNS analyser on samples dried under vacuum. Thermogravimetric measurements were carried out with a Mettler Toledo TGA/SDTA 851e apparatus.

X-ray Crystallographic Studies: X-ray diffraction data of **7** and **8** were collected at room temperature with a Nonius KappaCCD diffractometer using a graphite-monochromated Mo-K_α radiation source (λ = 0.71073 Å). The Denzo and Scalepack[43] programs were used for cell refinements and data reduction. The structures were solved by direct methods using the SIR97[44] program with the WinGX[45] graphical user interface. The structural refinements were carried out with SHELX-97.[46] All nonhydrogen atoms were refined anisotropically. A multiscan absorption correction, based on equivalent reflections, was applied to the data using the program SORTAV[47] ($T_{max.}/T_{min.}$ 0.8972/0.5899 for **7** and 0.995/0.898 for **8**). H atoms of water molecules were found from difference maps and were positionally refined with geometric restraints (O−H 0.82 Å and H···H 1.30 Å) and with U_{iso}(H) = 1.2U_{eq}(O). The remaining H atoms were placed in calculated positions and refined using a riding model with C−H = 0.97 Å and U_{iso}(H) = 1.2U_{eq}(C). All nonhydrogen atoms were refined anisotropically. Crystallographic data are summarised in Table 2.

CCDC-149375 and -236227 contain the supplementary crystallographic data for this paper. These data can be obtained free of charge via www.ccdc.cam.ac.uk/conts/retrieving.html (or from the Cambridge Crystallographic Data Centre, 12 Union Road, Cambridge CB2 1EZ, UK; fax: (internat.) +44-1223-336-033; E-mail: deposit@ccdc.cam.ac.uk).

Supporting Information (see also the footnote on the first page of this article): Figures S1−S3 show χT vs. T plots for compounds **1**−**3** and **5**−**6**. Figures S4 and S5 show, respectively, the EPR spectra of *p*-rad[CoCr(ox)$_3$]·2H$_2$O (**2**) and *p*-rad[NiCr(ox)$_3$]·H$_2$O (**3**) at different temperatures.

Table 2. Crystal data and structure refinement for **7**−**8**

Compound	**7**	**8**
Empirical formula	$C_{19}H_{25}CrMnN_3O_{17}$	$C_{19}H_{27}CrMnN_3O_{18}$
Molecular mass	674.36	692.38
a (Å)	11.343(2)	8.7890(2)
b (Å)	14.311(2)	11.5290(2)
c (Å)	16.928(10)	14.4980(3)
α (°)	90	89.1000(8)
β (°)	104.14(3)	82.2150(9)
γ (°)	90	70.8690(9)
Z	2	2
d (Mg·m^{-3})	1.681	1.673
Crystal system	monoclinic	triclinic
Space group	C_c	$P\bar{1}$
Crystal dimensions (mm)	0.61 × 0.19 × 0.12	0.32 × 0.12 × 0.05
T (K)	293(2)	225(2)
Θ Range	4.68 < 2Θ < 61.24	2.84 < 2Θ < 57.42
Reflections collected	11092	34160
Independent reflections	6821	7040
Data/restraints/parameters	6821/2/402	7040/14/408
Final R indices [$I > 2\sigma(I)$]	R_1 = 0.0309, wR_2 = 0.0603	R_1 = 0.0507, wR_2 = 0.1058
R indices (all data)	R_1 = 0.0463, wR_2 = 0.0642	R_1 = 0.1391, wR_2 = 0.1417

Acknowledgments

This work was supported by the Ministerio de Ciencia y Tecnología (MCyT) (Project no. MAT2001-3507-C02-01). CGS and FMR acknowledge research contracts from MCyT (Programa "Ramón y Cajal"). We also thank J. M. Martínez-Agudo for his help with the magnetic measurements and thermogravimetric analysis.

[1] O. Kahn, *Molecular Magnetism*, Wiley-VCH, Weinheim, **1993**.
[2] For an overview of the richness of structural design in molecular magnetism see the Proceedings of the 8th International Conference on Molecule-based Magnets: *Polyhedron* **2003**, *14*−*17*, 1725−2584.
[3] H. Tamaki, Z. J. Zhong, N. Matsumoto, S. Kida, M. Koikawa, N. Achiwa, Y. Hashimoto, H. Okawa, *J. Am. Chem. Soc.* **1992**, *114*, 6974−6979.
[4] S. Decurtins, H. W. Schmalle, P. Schneuwly, H. R. Oswald, *Inorg. Chem.* **1993**, *32*, 1888−1892.
[5] S. Decurtins, H. W. Schmalle, H. R. Oswald, A. Linden, J. Ensling, P. Gütlich, A. Hauser, *Inorg. Chim. Acta* **1994**, *216*, 65−73.
[6] S.G. Carling, C. Mathonière, P. Day, K. M. A. Malik, S. J. Coles, M. B. Hursthouse, *J. Chem. Soc., Dalton Trans.* **1996**, 1839−1843.
[7] R. Pellaux, H. W. Schmalle, R. Huber, P. Fischer, T. Hauss, B. Ouladdiaf, S. Decurtins, *Inorg. Chem.* **1997**, *36*, 2301−2308.
[8] S. Decurtins, H. W. Schmalle, P. Schneuwly, J. Ensling, P. Gütlich, *J. Am. Chem. Soc.* **1994**, *116*, 9521.
[9] S. Decurtins, H. W. Schmalle, R. Pellaux, R. Huber, P. Fischer, B. Ouladdiaf, *Adv. Mater.* **1996**, *8*, 647−651.
[10] S. Decurtins, H. W. Schmalle, R. Pellaux, *New J. Chem.* **1998**, *22*, 117−121.
[11] R. Andrés, M. Gruselle, B. Malézieux, M. Verdaguer, J. Vaissermann, *Inorg. Chem.* **1999**, *38*, 4637−4646.
[12] G. L. J. A. Rikken, E. Raupach, *Nature* **1997**, *390*, 493−494.
[13] E. Coronado, J. R. Galán-Mascarós, C. J. Gómez-García, J. M. Martínez-Agudo, *Inorg. Chem.* **2001**, *40*, 113−120.
[14] M. Clemente-León, E. Coronado, J. R. Galán-Mascarós, C. J. Gómez-García, *Chem. Commun.* **1997**, 1727.

[15] E. Coronado, J. R. Galán-Mascarós, C. J. Gómez-García, J. Ensling, P. Gütlich, *Chem. Eur. J.* **2000**, *6*, 552−563.
[16] P. G. Lacroix, I. Malfant, S. Benard, P. Yu, E. Riviere, K. Nakatani, *Chem. Mater.* **2001**, *13*, 441−449.
[17] E. Coronado, J. R. Galán-Mascarós, C. J. Gómez-García, V. Laukhin, *Nature* **2000**, *408*, 447−449.
[18] M. Deumal, J. Cirujeda, J. Veciana, J. J. Novoa, *Chem. Eur. J.* **1999**, *5*, 1631−1642.
[19] A. Caneschi, D. Gatteschi, R. Sessoli, P. Rey, *Acc. Chem. Res.* **1989**, *22*, 392−398.
[20] A. Caneschi, D. Gatteschi, P. Rey, *Prog. Inorg. Chem.* **1991**, *39*, 331−429.
[21] K. Fegy, D. Luneau, T. Ohm, C. Paulsen, P. Rey, *Angew. Chem.* **1998**, *110*, 1331−1335; *Angew. Chem. Int. Ed.* **1998**, *37*, 1270−1273.
[22] K. Awaga, T. Inabe, U. Nagashima, T. Nakamura, M. Matsumoto, Y. Kawabata, Y. Maruyama, *Chem. Lett.* **1991**, 1777−1780.
[23] A. Yamaguchi, K. Awaga, T. Inabe, T. Nakamura, M. Matsumoto, Y. Maruyama, *Chem. Lett.* **1993**, 1443−1446.
[24] A. Yamaguchi, T. Okuno, K. Awaga, *Bull. Chem. Soc. Jpn.* **1996**, *69*, 875−882.
[25] C. Michaut, L. Ouahab, P. Bergerat, O. Kahn, A. Bousseksou, *J. Am. Chem. Soc.* **1996**, *118*, 3610−3616.
[26] H. Imai, T. Otsuka, T. Naito, K. Awaga, T. Inabe, *J. Am. Chem. Soc.* **1999**, *121*, 8098−8103.
[27] H. O. Stumpf, L. Ouahab, Y. Pei, D. Grandjean, O. Kahn, *Science* **1993**, *261*, 447.
[28] H. O. Stumpf, L. Ouahab, Y. Pei, P. Bergerat, O. Kahn, *J. Am. Chem. Soc.* **1994**, *116*, 3866−3874.
[29] M. G. F. Vaz, L. M. M. Pinheiro, H. O. Stumpf, A. F. C. Alcântara, S. Golhen, L. Ouahab, O. Cador, C. Mathonière, O. Kahn, *Chem. Eur. J.* **1999**, *5*, 1486−1495.
[30] G. Ballester, E. Coronado, C. Giménez-Saiz, F. M. Romero, *Angew. Chem. Int. Ed.* **2001**, *40*, 792−795.
[31] U. Geiser, B. L. Ramakrishna, R. D. Willett, F. B. Hulsbergen, J. Reedijk, *Inorg. Chem.* **1987**, *26*, 3750.
[32] H. Oshio, U. Nagashima, *Inorg. Chem.* **1992**, *31*, 3295−3301.
[33] G. Marinescu, M. Andruh, R. Lescouëzec, M. C. Muñoz, J. Cano, F. Lloret, M. Julve, *New J. Chem.* **2000**, *24*, 527−536.
[34] S. Decurtins, M. Gross, H. W. Schmalle, S. Ferlay, *Inorg. Chem.* **1998**, *37*, 2443−2449.
[35] D. J. Price, A. K. Powell, P. T. Wood, *J. Chem. Soc., Dalton Trans.* **2000**, 3566−3569.
[36] R. Lescouëzec, J. Vaissermann, L. M. Toma, R. Carrasco, F. Lloret, M. Julve, *Inorg. Chem.* **2004**, *43*, 2234−2236.
[37] M. Drillon, E. Coronado, D. Beltrán, R. Georges, *Chem. Phys.* **1983**, *79*, 449.
[38] The total spin Hamiltonian is the sum of exchange and Zeeman terms. The latter includes also the contribution of the radical: $H = H_{ex} - g\mu_B \mathbf{H}(S_A + S_B + S_{rad})$.
[39] For a review on molecular spin ladders, see: C. Rovira, *Chem. Eur. J.* **2000**, *6*, 1723−1729.
[40] The program MAGPACK was used for the calculation of the spin states and thermodynamic properties: J. J. Borrás-Almenar, J. M. Clemente-Juan, E. Coronado, B. S. Tsukerblat, *J. Comput. Chem.* **2001**, *22*, 985.
[41] R. Karthein, H. Motschi, A. Schweiger, S. Ibric, B. Sulzberger, W. Stumm, *Inorg. Chem.* **1991**, *30*, 1606−1611.
[42] V. Laget, C. Hornick, P. Rabu, M. Drillon, P. Turek, R. Ziessel, *Adv. Mater.* **1998**, *10*, 1024−1028.
[43] Z. Otwinowski, W. Minor, *Methods in Enzymology* **1997**, *276*, 307.
[44] A. Altomare, M. C. Burla, M. Camalli, G. Cascarano, C. Giacovazzo, A. Guagliardi, A. G. G. Moliterni, G. Polidori, R. Spagna, *J. Appl. Cryst.* **1999**, *32*, 115.
[45] L. J. Farrugia, *J. Appl. Cryst.* **1999**, *32*, 837.
[46] G. M. Sheldrick, SHELX-97, an integrated system for solving and refining crystal structures from diffraction data, University of Göttingen (Germany), **1997**.
[47] R. H. Blessing, *J. Appl. Cryst.* **1997**, *30*, 421.

Received August 8, 2004
Early View Article
Published Online November 24, 2004

